

On stratification, barotropic tides, and secular changes in surface tidal elevations: Two-layer analytical model

Alfredo N. Wetzel *

*Applied and Interdisciplinary Mathematics Program, Department of Mathematics, University of
Michigan, Ann Arbor, Michigan*

Brian K. Arbic

Department of Earth and Environmental Sciences, University of Michigan, Ann Arbor, Michigan

Ivana Cerovecki and Myrl C. Hendershott

*Physical Oceanography Research Division, Scripps Institution of Oceanography, University of
California, San Diego, California*

Richard H. Karsten

Department of Mathematics and Statistics, Acadia University, Wolfville, Nova Scotia, Canada

Peter D. Miller

Department of Mathematics, University of Michigan, Ann Arbor, Michigan

Joseph F. Molinari

Department of Mathematics, Florida State University, Tallahassee, Florida

**Corresponding author address:* Alfredo N. Wetzel, Department of Mathematics, 5080 East Hall,
530 Church Street, University of Michigan, Ann Arbor, MI, 48109-1043.

E-mail: wreagan@umich.edu

ABSTRACT

In this study the influence of stratification on surface tidal elevations in a two-layer analytical model is examined. The model assumes linearized, non-rotating, shallow-water dynamics in one dimension with astronomical forcing and allows for arbitrary topography. Using a natural modal separation, both large scale (barotropic) and small scale (baroclinic) components of the surface tidal elevation are shown to be comparably affected by stratification. It is also shown that the topography and basin boundaries affect the sensitivity of the barotropic surface tide to stratification significantly. This paper, therefore, provides a framework to understand how the presence of stratification impacts barotropic as well as baroclinic tides, and how climatic perturbations to oceanic stratification contribute to secular variations in tides. Results from a realistic-domain global numerical two-layer tide model are briefly examined and found to be qualitatively consistent with the analytical model results.

1. Introduction

In this paper we utilize an analytical model to examine the impact of deep ocean stratification and climatic perturbations to this stratification on both large-horizontal scale (barotropic) and small-horizontal scale (baroclinic) components of the surface tidal elevations. Numerous studies have determined that, at specific locations, surface tidal elevations have undergone secular changes over the last century (e.g., Cartwright 1971; Woodworth et al. 1991; Flick et al. 2003; Colosi and Munk 2006; Ray 2006, 2009; Jay 2009; Woodworth 2010; Müller et al. 2011; Zaron and Jay 2014). One motivation for this work arises from the possibility that these observed secular signals are caused in part by changes in the oceanic stratification.

Another motivation for this work is to explain why the addition of stratification alters the large-horizontal scale (barotropic) tide in realistic-domain global numerical simulations at the same time that, as is well known, it introduces a small-scale (baroclinic) tide. Arbic et al. (2004) briefly noted that the dominant large amplitude, large-horizontal scale (barotropic) tide in a two-layer global model is distinct from the barotropic tide in a one-layer global model; see Figure 10 in that paper. The large-scale amplitudes of the one- and two-layer results differ by roughly 10%, while the phases differ by about 10° . The shift in barotropic tides with the addition of stratification into a realistic-domain global model can also be seen in Figure 1 of Shriver et al. (2014). In this paper we investigate whether a simple analytical model can produce qualitatively similar results as seen in these global numerical simulations run in realistic domains.

Our study is global in nature. Related regional studies include Kang et al. (2002), who examined seasonal changes in stratification and tides in the Yellow and East China Seas, and Colosi and Munk (2006), who examined the impact of internal tides on the secular variations in surface tidal elevations recorded in tide gauges. Another study related to the present one is Müller (2012), who

examined the effects of seasonally varying coastal stratifications on the tides using an idealized model.

The underlying mechanism examined here for the impact of stratification on barotropic tides is that stratification introduces a perturbation to barotropic gravity wave speeds (Gill 1982). This mechanism for the impact of stratification on barotropic tides differs from the mechanism examined by Müller (2012), which involves eddy viscosities rather than gravity wave speeds and is oriented towards the shelves rather than the deep ocean.

The analytical model used in this paper assumes two-layer, linearized, non-rotating, shallow-water dynamics in one horizontal dimension. We assume astronomical forcing and allow for arbitrary bottom topography in both finite and infinite basin geometries. For convenience, all numerical results in this paper utilize a topography consisting of a Gaussian bump in the center of the basin. Baroclinic tides are generated by barotropic tidal flow over the topographic feature. We impose no-normal flow boundary conditions at the basin boundaries for a finite basin, or equivalently decay to zero at infinity for the infinite basin. We obtain model solutions using both a Fourier series and a Neumann series expansion. Importantly, the Neumann series contains built in barotropic and baroclinic modes allowing both the velocities and elevations to be naturally decomposed.

We examine the effects of stratification on the surface elevations primarily by computing the surface elevations for different stratification parameters on both finite and infinite basin geometries. Quite visible in these results, at least for the finite basin, is a measurable change in the barotropic as well as baroclinic components of the surface elevation, brought about by changes in stratification. In addition, we find that the effects of stratification on the barotropic component of surface elevation are significantly influenced by the topography and basin boundaries.

2. Illustrative global numerical simulations

To illustrate the effects of stratification on barotropic tides, and to motivate our analytical model, we briefly discuss numerical one- and two-layer tide simulations performed in a realistic near-global domain. The simulations are executed with the Hallberg Isopycnal Model (HIM; Hallberg and Rhines 1996) on a $1/8^\circ$ grid and a multiplicative topographic wave drag factor of 5, where the wave drag acts only in waters deeper than 1000 m. This topographic drag factor is chosen to minimize the discrepancy in deep-ocean tidal elevations in the tide model and the GOT99 satellite-altimeter constrained tide model (Ray 1999) and yields a 6.69 cm error in our one-layer $1/8^\circ$ run. As in Arbic et al. (2004), the wave drag acts only on the bottom flow in our two-layer simulations. For simplicity, we apply only astronomical forcing for M_2 , the principal lunar semidiurnal tide. The self-attraction and loading term is computed iteratively using the full spherical harmonic treatment (Hendershott 1972). We refer the interested reader to Arbic et al. (2004) for further details on the model setup and parameters.

We evaluate the strength of the baroclinic tides in the $1/8^\circ$ HIM results utilized in this paper via the same methods used to evaluate the $1/12^\circ$ HYCOM (HYbrid Coordinate Ocean Model) results in Arbic et al. (2010). In the HIM “interface perturbation” run to be described shortly, we find that the root mean square (RMS) M_2 internal tide perturbations to sea surface elevations, averaged over a large box around Hawai’i 35 degrees in latitude by 50 degrees in longitude, are 0.64 cm for amplitude and 3.56 degrees for phase. These numbers compare well to the 0.87 cm and 4.35 degree perturbations estimated in the same box from the along-track satellite altimeter observations of Ray and Mitchum (1996, 1997). The $1/8^\circ$ “ g' perturbation” and “control” runs to be described shortly yield very similar numbers. Therefore the $1/8^\circ$ two-layer HIM simulations produce internal tides that are of comparable magnitudes to those in observations.

Figures 1 and 2 display the impacts of stratification, and of perturbations to stratification, on the tidal amplitude and phase. Figure 1(a) displays the global M_2 surface elevation amplitude in our $1/8^\circ$ one-layer control simulation. Figure 1(b) displays the difference in surface elevation amplitudes between the $1/8^\circ$ two-layer control simulation, having an interface at 700 m and reduced gravity of $g' = 1.64 \times 10^{-2} \text{ m s}^{-2}$, and the one-layer control simulation. Differences between the two- and one-layer simulations are clearly seen in the large-scale barotropic tides as well as in the introduction of small-scale barotropic tides. A perturbation to the stratification in the two-layer numerical model, either in the form of an interface lying at 800 m rather than 700 m, or in an increase in g' to $1.78 \times 10^{-2} \text{ m s}^{-2}$, leads to further alterations in both the large-scale barotropic and small-scale baroclinic tides; see Figures 1(c) and (d). Our choices of reduced gravity g' and interface values are explained in section 5 a. Figure 2 demonstrates that changes also take place in phase, when first stratification and second climatically perturbed stratifications are introduced into the model. Figures 1 and 2 demonstrate that the change in the barotropic tide due to stratification is a robust effect. A more detailed examination of the numerical results, and comparison to observed secular changes, is reserved for a paper in preparation.

3. Governing equations

Let $u_1(x, t)$, $u_2(x, t)$, $\eta_1(x, t)$, $\eta_2(x, t)$ be, respectively, the upper and lower layer velocities and the perturbation surface and internal elevations (displacements), where x denotes the spatial coordinate and t denotes time. Let the resting layer depths be H_1 and $h_2(x)$, where subscripts 1 and 2 denote the upper and lower layers, respectively. Assuming linearized, non-rotating, shallow-water dynamics in one dimension with astronomical forcing yields the upper and lower layer mass conservation equations

$$\frac{\partial}{\partial t}(\eta_1 - \eta_2) + H_1 \frac{\partial u_1}{\partial x} = 0, \quad (1)$$

$$\frac{\partial \eta_2}{\partial t} + \frac{\partial}{\partial x} [h_2(x)u_2] = 0, \quad (2)$$

respectively, and the upper and lower layer momentum equations

$$\frac{\partial u_1}{\partial t} = -g \frac{\partial \eta_1}{\partial x} + g \frac{\partial}{\partial x} \eta_0 e^{i(kx+\omega t)} - r_1 u_1, \quad (3)$$

$$\frac{\partial u_2}{\partial t} = (g' - g) \frac{\partial \eta_1}{\partial x} - g' \frac{\partial \eta_2}{\partial x} + g \frac{\partial}{\partial x} \eta_0 e^{i(kx+\omega t)} - r_2 u_2, \quad (4)$$

respectively. Here g denotes gravity, $g' = g(\rho_2 - \rho_1)/\rho_2$ is the reduced gravity with ρ_1 and ρ_2 being the upper and lower layer densities (note $\rho_1 \leq \rho_2$), r_1 and r_2 are damping rates on the upper and lower layer flows, respectively, and the astronomical forcing is given by $\eta_0 e^{i(kx+\omega t)}$, where η_0 , k , and ω are the amplitude, wavenumber, and frequency of the forcing. A sketch of the model is given in Figure 3.

We impose the no-normal flow boundary conditions

$$u_1(L_1, t) = u_1(L_2, t) = u_2(L_1, t) = u_2(L_2, t) = 0, \quad (5)$$

where L_1 and L_2 are the basin boundaries. For an infinite basin we impose a decay condition on $u_1(x, t)$ and $u_2(x, t)$; a modification of (5) with the understanding that $L_1 \rightarrow -\infty$ and $L_2 \rightarrow \infty$.

We non-dimensionalize the governing equations using:

$$x = Lx^*, \quad t = t^*/\omega, \quad \eta_j = \eta_0 \eta_j^*, \quad u_j = \eta_0 \sqrt{\frac{g}{H_1 + H_2}} u_j^*, \quad h_2 = H_2 [1 - \sigma b^*(x^*)], \quad (6)$$

where the asterisks denote non-dimensional variables, and $j = 1, 2$. The parameter L is a characteristic length of the system, e.g. the basin size in a finite basin, or a topographical length scale in an infinite basin. The quantity $\sigma b^*(x^*)$ is a non-dimensionalization of the bottom topography such that $0 \leq b^* < 1$ and σ is a scaling parameter. Hence, the quantity H_2 is the maximum value attained by h_2 in the given domain.

The non-dimensional governing equations, after dropping the asterisks, are

$$\frac{\partial}{\partial t}(\eta_1 - \eta_2) + \varepsilon \gamma \frac{\partial u_1}{\partial x} = 0, \quad (7)$$

$$\frac{\partial \eta_2}{\partial t} + \varepsilon(1 - \gamma) \frac{\partial}{\partial x} [(1 - \sigma b)u_2] = 0, \quad (8)$$

$$\frac{\partial u_1}{\partial t} + \varepsilon \frac{\partial \eta_1}{\partial x} + \delta_1 u_1 = \varepsilon \frac{\partial}{\partial x} \left[e^{i(\phi x + t)} \right], \quad (9)$$

$$\frac{\partial u_2}{\partial t} + \varepsilon \frac{\partial}{\partial x} [(1 - \alpha)\eta_1 + \alpha\eta_2] + \delta_2 u_2 = \varepsilon \frac{\partial}{\partial x} \left[e^{i(\phi x + t)} \right], \quad (10)$$

where the governing non-dimensional parameters are

$$\varepsilon = \frac{\sqrt{g(H_1 + H_2)}}{\omega L}, \quad \gamma = \frac{H_1}{H_1 + H_2}, \quad \alpha = \frac{g'}{g}, \quad \delta_1 = \frac{r_1}{\omega}, \quad \delta_2 = \frac{r_2}{\omega}, \quad \phi = kL. \quad (11)$$

Thus, δ_1, δ_2 are the damping parameters and α, γ are the two stratification parameters. By definition $0 \leq \alpha < 1$, where $\alpha = 0$ represents unstratified flow. Similarly, by definition, $0 \leq \gamma \leq 1$. The parameters ε and ϕ are measures of the forcing period and wavenumber. The boundary conditions simply become

$$u_1(\ell_1, t) = u_1(\ell_2, t) = u_2(\ell_1, t) = u_2(\ell_2, t) = 0, \quad (12)$$

where $\ell_1 = L_1/L$ and $\ell_2 = L_2/L$.

In the open ocean, since tidal flows are relatively weak, the quadratic bottom boundary layer drag is also weak (Munk 1997). We assume that bottom drag in the open ocean is dominated by topographic internal wave drag (Jayne and St. Laurent 2001; Arbic et al. 2004; Egbert et al. 2004, among others). In our treatment we allow drag on the upper layer flow as a convenience that proves useful in examining limiting cases; we believe that the bottom drag-only case ($\delta_1 = 0$) is more relevant for the ocean. We note also that the g' term in front of the derivative of η_1

in equation (4) arises from the fact that we do not make the Boussinesq approximation when deriving these equations. It is worth noting that had we assumed the Boussinesq approximation, the effects of stratification on the barotropic and baroclinic surface tides would be qualitatively similar. The differences between Boussinesq and non-Boussinesq solutions, however, will not be pursued further in this paper.

Note that, in the absence of topography, setting $\alpha = 0$ and $\delta_1 = \delta_2$ yields the governing equations in the one-layer shallow water model used in Arbic et al. (2009). This follows from the fact that if we set $\alpha = 0$ (so that the layer densities are equal) and $\delta_1 = \delta_2$ (equal damping rates in the two layers), then the momentum equations for both u_1 and u_2 are identical to the momentum equation in the one-layer case.

4. Analytical solution

To solve the two-layer system (7)–(10), we assume a separable solution of the form

$$u_1 = U_1(x)e^{it}, \quad u_2 = U_2(x)e^{it}, \quad \eta_1 = N_1(x)e^{it}, \quad \eta_2 = N_2(x)e^{it}. \quad (13)$$

This recovers the steady-state solution, which is stable provided there is damping. Substituting these into the mass equations (7), (8) and solving for N_1, N_2 gives the system

$$N_1(x) = i\varepsilon\gamma U_1' + i\varepsilon(1 - \gamma)[(1 - \sigma b)U_2]', \quad (14)$$

$$N_2(x) = i\varepsilon(1 - \gamma)[(1 - \sigma b)U_2]'. \quad (15)$$

Except for g' , prime notation denotes derivatives of a function with respect to x here and in the rest of the paper. This system can be written concisely in matrix form as

$$\mathbf{N}(x) = i\varepsilon(\mathbb{I} + \mathbf{e}_{12})\mathbf{\Gamma}\mathbf{U}'(x), \quad (16)$$

where $\mathbf{N}(x) = \begin{bmatrix} N_1 \\ N_2 \end{bmatrix}$, $\mathbb{I} = \begin{bmatrix} 1 & 0 \\ 0 & 1 \end{bmatrix}$ is the identity matrix, $\mathbf{e}_{12} = \begin{bmatrix} 0 & 1 \\ 0 & 0 \end{bmatrix}$, $\mathbf{\Gamma} = \begin{bmatrix} \gamma & 0 \\ 0 & 1-\gamma \end{bmatrix}$, and $\mathbf{U}(x) = (\mathbb{I} - \sigma b \mathbf{e}_{22}) \begin{bmatrix} U_1 \\ U_2 \end{bmatrix} = \begin{bmatrix} U_1 \\ (1-\sigma b)U_2 \end{bmatrix}$ with $\mathbf{e}_{22} = \begin{bmatrix} 0 & 0 \\ 0 & 1 \end{bmatrix}$. Similarly, with the use of equations (14) and (15), substituting (13) into the momentum equations (9) and (10) gives

$$s_1 U_1 + U_1'' + \left(\frac{1-\gamma}{\gamma} \right) [(1-\sigma b) U_2]'' = \frac{\phi}{\varepsilon \gamma} e^{i\phi x}, \quad (17)$$

$$s_2 U_2 + (1-\alpha) \left(\frac{\gamma}{1-\gamma} \right) U_1'' + [(1-\sigma b) U_2]'' = \frac{\phi}{\varepsilon (1-\gamma)} e^{i\phi x}, \quad (18)$$

where $s_1 = \frac{1-i\delta_1}{\varepsilon^2 \gamma}$ and $s_2 = \frac{1-i\delta_2}{\varepsilon^2 (1-\gamma)}$. Multiplying (17) by s_2 and (18) by s_1 allows us to write these equations as

$$\mathbf{A} \mathbf{U}(x) + \sigma \mathbf{A} \mathbf{e}_{22} \left(\frac{b(x)}{1-\sigma b(x)} \right) \mathbf{U}(x) + \mathbf{B} \mathbf{U}''(x) = \mathbf{F}(x), \quad (19)$$

where

$$\mathbf{A} = s_1 s_2 \mathbb{I}, \quad \mathbf{B} = \begin{bmatrix} s_2 & s_2 \left(\frac{1-\gamma}{\gamma} \right) \\ s_1 (1-\alpha) \left(\frac{\gamma}{1-\gamma} \right) & s_1 \end{bmatrix}, \quad \text{and} \quad \mathbf{F}(x) = \frac{\phi}{\varepsilon} \begin{bmatrix} \frac{s_2}{\gamma} \\ \frac{s_1}{1-\gamma} \end{bmatrix} e^{i\phi x}. \quad (20)$$

In the subsequent subsections we present three distinct methods, each having different strengths, to solve this set of equations. First, we show the derivation of a Fourier series solution. This solution method is limited to the finite basin problem, but is simple to implement and is robust numerically. Second, we introduce a Neumann series solution. The Neumann series solution is numerically sensitive to the topography, but suggests an analytically valuable decomposition into barotropic and baroclinic modes. Lastly, we introduce a scattering solution to the problem. We include the scattering solution method here because it bears similarities to the internal tide generation problem of great recent interest to the community (e.g., Llewellyn Smith and Young 2001; St. Laurent et al. 2003; Khatiwala 2003). The scattering solution is, however, not emphasized in this paper as much as the other two methods because, first, the finite basin is more realistic than the

infinite basin, and second, the scattering solution still requires prior knowledge of the “incident” barotropic tidal velocity on the topography; whereas we are interested in obtaining, without prior assumptions, the full barotropic and baroclinic tidal solution.

a. Fourier series solution

In the finite basin case, we can construct a solution for general topography using Fourier series. Here we non-dimensionalize using the basin width, making $\ell_1 = -1, \ell_2 = 0$. To satisfy the boundary conditions the velocities must be expansions of sines only, i.e,

$$U_1(x) = \sum_{n=1}^{\infty} c_n \sin n\pi x, \quad U_2(x) = \sum_{n=1}^{\infty} d_n \sin n\pi x, \quad (1 - \sigma b(x))U_2(x) = \sum_{n=1}^{\infty} e_n \sin n\pi x, \quad (21)$$

where

$$e_n = 2 \int_{-1}^0 (1 - \sigma b(x)) U_2(x) \sin(n\pi x) dx = d_n - \sum_{m=1}^{\infty} d_m \sigma_{mn} \quad (22)$$

with

$$\sigma_{mn} = 2\sigma \int_{-1}^0 b(x) \sin(m\pi x) \sin(n\pi x) dx. \quad (23)$$

We may also write the forcing term in a Fourier series expansion. That is,

$$e^{i\phi x} = \sum_{n=1}^{\infty} f_n \sin n\pi x, \quad (24)$$

where

$$f_n = 2 \int_{-1}^0 e^{i\phi x} \sin(n\pi x) dx = \frac{2n\pi[1 - (-1)^n e^{-i\phi}]}{\phi^2 - (n\pi)^2}. \quad (25)$$

Therefore, equations (17) and (18) can be written in terms of the coefficients c_n and d_n as

$$((n\pi)^2 - s_1) c_n + (n\pi)^2 \left(\frac{1 - \gamma}{\gamma} \right) d_n = (n\pi)^2 \left(\frac{1 - \gamma}{\gamma} \right) \sum_{m=1}^{\infty} d_m \sigma_{mn} - \frac{\phi}{\varepsilon \gamma} f_n, \quad (26)$$

$$(n\pi)^2 (1 - \alpha) \left(\frac{\gamma}{1 - \gamma} \right) c_n + ((n\pi)^2 - s_2) d_n = (n\pi)^2 \sum_{m=1}^{\infty} d_m \sigma_{mn} - \frac{\phi}{\varepsilon (1 - \gamma)} f_n. \quad (27)$$

Solving this system for the coefficients c_n and d_n gives

$$c_n = \frac{s_2}{D_n} \left(\frac{1-\gamma}{\gamma} \right) \left[\frac{\phi}{\varepsilon(1-\gamma)} f_n - (n\pi)^2 \sum_{m=1}^{\infty} d_m \sigma_{mn} \right], \quad (28)$$

$$d_n = \frac{s_1 - \alpha(n\pi)^2}{D_n} \left[\frac{\phi}{\varepsilon(1-\gamma)} f_n - (n\pi)^2 \sum_{m=1}^{\infty} d_m \sigma_{mn} \right], \quad (29)$$

where

$$D_n = s_1 s_2 - (s_1 + s_2) (n\pi)^2 + \alpha(n\pi)^4. \quad (30)$$

Note that we have written the bottom topography as an extra “forcing” term. Indeed, equation (29) for d_n may be viewed as an infinite system of linear equations. To highlight this fact, it can be written as $\mathbf{M}\mathbf{d} = \mathbf{f}$, where

$$\mathbf{M}_{nm} = \begin{cases} D_n + (s_1 - \alpha(n\pi)^2)(n\pi)^2 \sigma_{nm} & \text{for } n = m \\ (s_1 - \alpha(n\pi)^2)(n\pi)^2 \sigma_{nm} & \text{for } n \neq m \end{cases}, \quad (31)$$

and

$$\mathbf{f}_n = (s_1 - \alpha(n\pi)^2) \frac{\phi}{\varepsilon(1-\gamma)} f_n. \quad (32)$$

For a finite number of modes this system can be solved directly for $\mathbf{d} = (d_1, d_2, \dots)$ by simply inverting the matrix \mathbf{M} . From this we may solve for the c_n and using equations (14), (15) we can calculate the elevations

$$N_1(x) = \sum_{n=1}^{\infty} a_n \cos n\pi x, \quad N_2(x) = \sum_{n=1}^{\infty} b_n \cos n\pi x, \quad (33)$$

with

$$a_n = i\varepsilon n\pi \left(\gamma c_n + (1-\gamma) \left(d_n - \sum_{m=1}^{\infty} d_m \sigma_{mn} \right) \right), \quad (34)$$

$$b_n = i\varepsilon n\pi (1-\gamma) \left(d_n - \sum_{m=1}^{\infty} d_m \sigma_{mn} \right). \quad (35)$$

b. Neumann series solution

For small enough topography, we can obtain a solution for both finite or infinite basins using a Green's function approach. This method is thus limited by the vertical scale of the topography, but provides a natural generalization to the infinite basin and gives a natural decomposition of the system into barotropic and baroclinic scales; this is discussed further in the next subsection. For the rest of this subsection we assume $\alpha \neq 0$, ensuring that \mathbf{B} is non-singular, and $\delta_1 \neq \delta_2$. Technical details aside, solutions for the one-layer case may be found by taking the limit $\alpha \rightarrow 0$.

We may nearly uncouple the system (19) by diagonalizing the matrix \mathbf{B} ; $\mathbf{B}\mathbf{V} = \mathbf{V}\mathbf{\Lambda}$, where $\mathbf{\Lambda}$ is a diagonal matrix of the eigenvalues of \mathbf{B} , in decreasing magnitude, and \mathbf{V} is a matrix with the respective eigenvectors. This allows us to change basis, left-multiplying the system by \mathbf{V}^{-1} , and rewrite (19) as

$$\mathbf{A}\mathbf{W}(x) + \mathbf{\Lambda}\mathbf{W}''(x) = \mathbf{V}^{-1}\mathbf{F}(x) - \sigma\mathbf{A}\mathbf{V}^{-1}\mathbf{e}_{22} \left(\frac{b(x)}{1 - \sigma b(x)} \right) \mathbf{V}\mathbf{W}(x), \quad (36)$$

which fully uncouples the left-hand side terms of (36). This is easily seen using the fact that \mathbf{A} commutes with any other matrix. The new variable $\mathbf{W}(x) = \begin{bmatrix} U^{BT}(x) \\ U^{BC}(x) \end{bmatrix} := \mathbf{V}^{-1}\mathbf{U}(x)$, which represents a separation of the system into large and small scale motions, can be thought of as representing the barotropic (BT) and baroclinic (BC) modes of the system. In this case, we associate the first term $U^{BT}(x)$ with the motions arising from the smaller of the eigenvalues (larger scales), we call this the barotropic mode, and the second term $U^{BC}(x)$ with the motions arising from the larger of the two eigenvalues (smaller scales), we call this the baroclinic mode. The reader should be warned that our definition of the separation may not be consistent with other definitions of the words barotropic and baroclinic in the literature.

We rewrite (36) as

$$\mathbf{E}\mathbf{W}(x) + \mathbf{W}''(x) = \mathbf{\Lambda}^{-1}\mathbf{V}^{-1}\mathbf{F}(x) - \sigma\mathbf{E}\mathbf{V}^{-1}\mathbf{e}_{22} \left(\frac{b(x)}{1 - \sigma b(x)} \right) \mathbf{V}\mathbf{W}(x), \quad (37)$$

where $\mathbf{E} := \mathbf{\Lambda}^{-1}\mathbf{A} = \begin{bmatrix} (k^{BT})^2 & 0 \\ 0 & (k^{BC})^2 \end{bmatrix}$. Note that k^{BT} and k^{BC} arise from the eigenvalues of \mathbf{B} and satisfy the polynomial equation

$$k^4 - \left(\frac{s_1 + s_2}{\alpha} \right) k^2 + \frac{s_1 s_2}{\alpha} = 0. \quad (38)$$

In the case $\alpha \ll 1$, typical for the ocean, it follows that $|k^{BT}| \ll |k^{BC}|$. In other words, k^{BT} and k^{BC} define two well separated scales for the problem. To avoid ambiguity about which solution of (38) we refer to, we pick those solutions such that $\text{Im}(k^{BT}), \text{Im}(k^{BC}) > 0$. That is, we label k^{BT} and k^{BC} the solutions of (38) in the upper half of the complex plane.

In the low damping regime ($\delta_1, \delta_2 \ll 1$), the polynomial (38) can be written in the approximate form

$$k^4 - \left(\frac{s_1 + s_2}{\alpha} \right) k^2 + \frac{s_1 s_2}{\alpha} \approx k^4 - \frac{k^2}{\varepsilon^2 \alpha \gamma (1 - \gamma)} + \frac{1}{\varepsilon^4 \alpha \gamma (1 - \gamma)} = 0. \quad (39)$$

Writing the equation in this manner clearly shows that in the low damping regime we essentially have one stratification parameter: $\alpha \gamma (1 - \gamma)$. For this reason, perturbations in α may lead to the same scales k^{BT} and k^{BC} as perturbations in γ . In particular, in the case $\gamma < 1/2$ which represents a thin upper layer over a thicker lower layer, a positive perturbation in α (increased density contrast) may lead to equivalent scales as a positive perturbation in γ (increased upper layer thickness). Lastly, it is worth noting that in this low damping regime equation (38) is equivalent to the formula for the phase speed of two superposed fluids with different density;

$$c^4 - g(H_1 + H_2)c^2 + gg'H_1H_2 = 0 \quad (40)$$

as given by Gill (1982) under the substitution $c = \omega L/k$.

The new system (37) can be readily solved using the Green's function of the problem

$$\mathbf{E}\mathbf{W}(x) + \mathbf{W}''(x) = \mathbf{f}(x), \quad (41)$$

where $\mathbf{f}(x)$ stands for the right-hand side of (37). The solution of (41) is given by

$$\mathbf{W}(x) = \int_{\ell_1}^{\ell_2} \mathbf{G}(x, y) \mathbf{f}(y) dy \quad \text{with} \quad \mathbf{G}(x, y) = \begin{bmatrix} g^{BT}(x, y) & 0 \\ 0 & g^{BC}(x, y) \end{bmatrix}, \quad (42)$$

where $\mathbf{G}(x, y)$, $\ell_1 < x, y < \ell_2$, satisfies the system

$$\mathbf{E}\mathbf{G}(x, y) + \mathbf{G}_{yy}(x, y) = \delta(y - x)\mathbb{I} \quad (43)$$

with boundary conditions

$$\mathbf{G}(x, \ell_1) = \mathbf{G}(x, \ell_2) = \mathbf{0}. \quad (44)$$

Note that $g^{BT}(x, y)$ is the Green's function arising from the barotropic mode, top equation of system (41), and $g^{BC}(x, y)$ is the Green's function arising from the baroclinic mode, bottom equation of system (41). Moreover, all information about the boundary conditions is contained in the Green's functions. This implies that we require different Green's functions for the finite and infinite basin cases. The Green's functions are

$$g(x, y) = \begin{cases} \frac{\sin k(x - \ell_1) \sin k(y - \ell_2)}{k \sin k(\ell_2 - \ell_1)} & x < y \\ \frac{\sin k(y - \ell_1) \sin k(x - \ell_2)}{k \sin k(\ell_2 - \ell_1)} & y < x \end{cases} \quad \text{and} \quad g(x, y) = \begin{cases} \frac{e^{ik(y-x)}}{2ik} & x < y \\ \frac{e^{ik(x-y)}}{2ik} & y < x \end{cases} \quad (45)$$

for a finite ($\ell_1 < \ell_2$) and infinite basin, respectively; see for example Greenberg (1971). In this case, k is a placeholder for k^{BT} or k^{BC} depending on whether $g(x, y)$ is meant to denote $g^{BT}(x, y)$ or $g^{BC}(x, y)$, respectively. Moreover, the construction of the Green's function for the infinite basin follows from the fact that we impose $\text{Im}(k) > 0$, as previously stated.

Now, with the adequate Green's functions for the basin in question, the solution method (42) allows us to write

$$\mathbf{W}(x) = \int_{\ell_1}^{\ell_2} \mathbf{D}(x, y) \mathbf{F}(y) dy - \sigma_{s_1 s_2} \int_{\ell_1}^{\ell_2} \mathbf{D}(x, y) \mathbf{e}_{22} \left(\frac{b(y)}{1 - \sigma b(y)} \right) \mathbf{VW}(y) dy, \quad (46)$$

where $\mathbf{D}(x, y) = \mathbf{G}(x, y) \mathbf{\Lambda}^{-1} \mathbf{V}^{-1}$. Letting

$$\mathbf{F}_0(x) := \int_{\ell_1}^{\ell_2} \mathbf{D}(x, y) \mathbf{F}(y) dy \quad (47)$$

and defining an operator K by

$$(K\mathbf{W})(x) := -s_1 s_2 \int_{\ell_1}^{\ell_2} \mathbf{D}(x, y) \mathbf{e}_{22} \left(\frac{b(y)}{1 - \sigma b(y)} \right) \mathbf{V} \mathbf{W}(y) dy \quad (48)$$

we can concisely write the equation (46) as $\mathbf{W}(x) = \mathbf{F}_0(x) + \sigma K \mathbf{W}(x)$. This last expression may be solved by the formal Neumann series

$$\mathbf{W}(x) = \mathbf{F}_0(x) + \sigma K \mathbf{F}_0(x) + \sigma^2 K^2 \mathbf{F}_0(x) + \dots \quad (49)$$

giving the full solution of $\mathbf{U}(x) = \mathbf{V} \mathbf{W}(x)$ in either a finite or infinite basin when the topography σ is small enough that the series (49) converges.

c. Separation into barotropic and baroclinic modes

A separation for the solution is suggested in the previous subsection. To make multiplication by \mathbf{V} completely determined we normalize the eigenvectors as presented in Flierl (1978) and Müller (2006). Essentially, for a given eigenvector $\mathbf{v} = (v_1, v_2)$ we impose the condition $\gamma v_1^2 + (1 - \gamma) v_2^2 = 1$; a depth weighted normalization. Under these assumptions we may write the matrix \mathbf{V} of eigenvectors as

$$\mathbf{V} = \begin{bmatrix} c^{BT}(1 - \gamma) & c^{BC}(1 - \gamma) \\ c^{BT} \gamma \left(\frac{s_1}{(k^{BT})^2} - 1 \right) & c^{BC} \gamma \left(\frac{s_1}{(k^{BC})^2} - 1 \right) \end{bmatrix}, \quad (50)$$

where

$$c^{BT, BC} = \frac{1}{\sqrt{(1 - \gamma) \gamma \left(1 - \gamma + \gamma \left(\frac{s_1}{(k^{BT, BC})^2} - 1 \right)^2 \right)}} \quad (51)$$

to satisfy the normalization conditions, and

$$\mathbf{V}^{-1} = \frac{1}{s_1} \left(\frac{1}{(k^{BT})^2} - \frac{1}{(k^{BC})^2} \right)^{-1} \begin{bmatrix} -\frac{1}{c^{BT}(1-\gamma)} \left(\frac{s_1}{(k^{BC})^2} - 1 \right) & \frac{1}{c^{BT}\gamma} \\ \frac{1}{c^{BC}(1-\gamma)} \left(\frac{s_1}{(k^{BT})^2} - 1 \right) & -\frac{1}{c^{BC}\gamma} \end{bmatrix}. \quad (52)$$

Thus, the matrix \mathbf{V} is invertible provided that $(k^{BT})^2 \neq (k^{BC})^2$. In the case when α is small the scales of the problem are well separated making \mathbf{V} invertible. We use the notation $c^{BT,BC}$ to mean that c^{BT} can be obtained by only using the first superscript in every term in the equation and c^{BC} by only using the second superscript. For example, in the case of c^{BT} we only use k^{BT} and for c^{BC} we only use k^{BC} . It may not be the case that the first superscript always refers to the barotropic mode; see the first term of equation (55) below.

For the layer elevations, a separation can be achieved simply by rewriting (16) as $\mathbf{N}(x) = i\mathcal{E}(\mathbb{I} + \mathbf{e}_{12})\mathbf{\Gamma}\mathbf{V}\mathbf{W}'(x)$. In this manner we can define the barotropic and baroclinic components of the surface and interfacial elevations as those arising from U^{BT} and U^{BC} , respectively. From matrix multiplication it follows that

$$N_1^{BT,BC} = i\mathcal{E}(1-\gamma)\gamma c^{BT,BC} \left(\frac{s_1}{(k^{BT,BC})^2} \right) \frac{dU^{BT,BC}}{dx}(x), \quad (53)$$

$$N_2^{BT,BC} = i\mathcal{E}(1-\gamma)\gamma c^{BT,BC} \left(\frac{s_1}{(k^{BT,BC})^2} - 1 \right) \frac{dU^{BT,BC}}{dx}(x). \quad (54)$$

The equations for U^{BT} and U^{BC} , equation (46), can similarly be written as

$$\begin{aligned} U^{BT,BC} = & \frac{1}{s_1 c^{BT,BC}} \left(\frac{1}{(k^{BT,BC})^2} - \frac{1}{(k^{BC,BT})^2} \right)^{-1} \left[\frac{\phi}{\gamma(1-\gamma)\mathcal{E}} \int_{\ell_1}^{\ell_2} g^{BT,BC} e^{i\phi y} dy \right. \\ & + \sigma(k^{BT,BC})^2 c^{BT} \left(1 - \frac{s_1}{(k^{BT})^2} \right) \int_{\ell_1}^{\ell_2} g^{BT,BC} U^{BT} \left(\frac{b}{1-\sigma b} \right) dy \\ & \left. + \sigma(k^{BT,BC})^2 c^{BC} \left(1 - \frac{s_1}{(k^{BC})^2} \right) \int_{\ell_1}^{\ell_2} g^{BT,BC} U^{BC} \left(\frac{b}{1-\sigma b} \right) dy \right]. \end{aligned} \quad (55)$$

We have written g^{BT} as opposed to $g^{BT}(x,y)$, b as opposed to $b(y)$, etc., to avoid clutter. It should be clear from context which terms are functions and which are parameters.

Equation (55) clearly shows that in the presence of topography there is mixing between the barotropic and baroclinic modes. Note that the barotropic solution U^{BT} depends in a non-trivial manner on the solution U^{BC} and that this coupling occurs only when the topography is non-zero, as shown in the last term of (55). On the other hand only the barotropic Green's function appears in the barotropic solution and only the baroclinic Green's function appears in the baroclinic solution. This corroborates that our splitting into barotropic and baroclinic modes is reasonable.

d. Scattering solution

A perturbation expansion with respect to the topographical parameter σ in equations (7)–(10) shows that the equations obtained at order σ for the infinite basin give the classical topographical scattering solution in terms of an incident velocity. That is, the σ order terms of the solution correspond to the scattering solution of the barotropic tide on the bottom roughness. The problem of internal wave generation from a bump that is impinged upon by a barotropic tidal velocity has received much attention in the oceanographic community; see for example Llewellyn Smith and Young (2001), St. Laurent et al. (2003), Khatiwala (2003). We briefly derive the scattering solution in this subsection to highlight its similarities with our full solution.

Consider expanding all variables in the problem in terms of the topographical parameter σ , i.e., $\varphi(x) \sim \varphi_0(x) + \sigma\varphi_1(x) + \dots$ for $\sigma \rightarrow 0$, where $\varphi(x)$ is the variable of interest. Gathering the order σ terms in equations (7)–(10), after using the separation (13), gives

$$i(N_1 - N_2) + \varepsilon\gamma U_1' = 0, \quad (56)$$

$$iN_2 + \varepsilon(1 - \gamma)U_2' = \varepsilon(1 - \gamma)F, \quad (57)$$

$$iU_1 + \varepsilon N'_1 + \delta_1 U_1 = 0, \quad (58)$$

$$iU_2 + (1 - \alpha)\varepsilon N'_1 + \alpha\varepsilon N'_2 + \delta_2 U_2 = 0, \quad (59)$$

where $F = \frac{\partial}{\partial x}(U_{2,0}b)$ with $U_{2,0}$ representing the incident tidal velocity on the topography or equivalently the $O(1)$ term in the expansion of U_2 . For the scattering problem, we assume that this background state $U_{2,0}$ is known and focus on solving for the higher order terms. Note that all variables in this equation correspond to the order σ terms, but we have dropped any indicative subscripts to avoid cumbersome notation. That is, in this subsection the notation N_1 really stands for $N_{1,1}$, the order σ term in the expansion of N_1 .

Since the system obtained is linear and has constant coefficients, we may readily solve the system above in the infinite basin case using the Fourier transform, e.g., $\hat{u}(k) = \int_{-\infty}^{\infty} u(x)e^{-ikx} dx$. Manipulating the equations this yields

$$(s_1 - k^2)\hat{N}_1 = s_1\hat{N}_2, \quad (60)$$

$$(s_2 - \alpha k^2)\hat{N}_2 - (1 - \alpha)k^2\hat{N}_1 = -i\varepsilon(1 - \gamma)s_2\hat{F}, \quad (61)$$

where s_1 and s_2 are as introduced previously. These equations may be combined to obtain

$$\left(k^4 - \left(\frac{s_1 + s_2}{\alpha}\right)k^2 + \frac{s_1 s_2}{\alpha}\right)\hat{N}_1 = -i\varepsilon(1 - \gamma)\frac{s_1 s_2}{\alpha}\hat{F}. \quad (62)$$

It is worth noting that the left-hand side of this equation is (38), making the separation of scales derived here identical to that in the previous section. This allows us to write equation (62) as

$$\hat{N}_1 = -i\varepsilon(1 - \gamma)(k^{BT})^2(k^{BC})^2 \left(\frac{1}{(k - k^{BT})(k + k^{BT})(k - k^{BC})(k + k^{BC})} \right) \hat{F} = \hat{R}_1 \hat{F}, \quad (63)$$

where k^{BT} and k^{BC} are the roots of the polynomial (38) as defined previously. Therefore, we obtain a closed form solution for $N_1(x)$ – the order σ term in the surface elevation – by taking the inverse Fourier transform on (63). The problem of inverting $\hat{N}_1(x)$ in equation (63) to obtain $N_1(x)$ is of course equivalent to taking a convolution of the functions $R_1(x)$ and $F(x)$. For this reason we seek a closed form solution of $R_1(x)$ since $F(x)$ is the known forcing function.

The integral $R_1(x) = \frac{1}{2\pi} \int_{-\infty}^{\infty} \hat{R}_1(k) e^{ikx} dk$ is readily done by summing residues separately for $x \geq 0$ and for $x < 0$ since k^{BT} and k^{BC} lie in the upper complex plane. In the case of $x \geq 0$ we close the contour of integration around the upper half plane leading to a positively oriented curve and in the case $x < 0$ we close the contour of integration around the lower half plane leading to a negatively oriented curve. After some manipulation we find $R_1(x) = R_1^{BT}(x) + R_1^{BC}(x)$, where

$$R_1^{BT}(x) = -\frac{\varepsilon(1-\gamma)}{2} \frac{e^{ik^{BT}|x|}}{k^{BT}} \left(\frac{1}{(k^{BT})^2} - \frac{1}{(k^{BC})^2} \right)^{-1} \quad (64)$$

and

$$R_1^{BC}(x) = \frac{\varepsilon(1-\gamma)}{2} \frac{e^{ik^{BC}|x|}}{k^{BC}} \left(\frac{1}{(k^{BT})^2} - \frac{1}{(k^{BC})^2} \right)^{-1}. \quad (65)$$

This separation of R_1 leads to a very natural way of writing the upper layer solution in terms of its barotropic and baroclinic components. Explicitly, we write

$$N_1^{BT}(x) = \int_{-\infty}^{\infty} R_1^{BT}(x-y) F(y) dy \quad \text{and} \quad N_1^{BC}(x) = \int_{-\infty}^{\infty} R_1^{BC}(x-y) F(y) dy \quad (66)$$

for the order σ barotropic and baroclinic components of the surface elevation, respectively.

Due to the fact that the scattering solution requires prior knowledge of the incident barotropic tide we do not include plots or analysis on it, but rather do so – in the next section – for the full solution.

5. Effects of stratification on the surface elevation

In this section we examine the impacts of stratification on surface tidal elevations in both the finite and infinite basin. We also examine the importance that topography and basin boundaries have on the value of the perturbed surface elevation. We utilize a suitably truncated versions of the Fourier series solution (33) and Neumann series solution (49) for several physically motivated trials.

a. Parameter values and description of trials

For the finite basin we impose boundaries at $\ell_1 = -1$, $\ell_2 = 0$ and for the infinite basin we assume that both boundaries lie at infinity. For the Neumann series, the only significant computational difference between the two basins lies in the different Green's functions employed; equation (45). For both basins we utilize an astronomical forcing with the parameter $\phi \approx 1.2827$, arising from $k = \frac{2}{6,371 \times 10^3} \text{ m}^{-1}$ (2π over the zonal wavelength of the semidiurnal tidal potential at the equator) and $L = 4,086 \times 10^3 \text{ m}$ (a typical ocean basin scale) as in Arbic et al. (2009); recall $\phi = kL$.

We choose a Gaussian topography of the form

$$b(x) = \frac{H_0}{H_2} e^{-(x+0.5)^2/a^2} \quad (67)$$

so that it is centered in the finite basin. The parameter a is chosen as $a = \frac{\pi}{2a_1L}$, where $a_1 = \omega \sqrt{(H_1 + H_2)/(g'H_1H_2)}$ is the topographic wavenumber that excites the first baroclinic mode in the absence of damping.

For all plots, except where noted, we use the forcing frequency $\omega = 1.405189 \times 10^{-4} \text{ s}^{-1}$ (the M_2 frequency), $H_1 = 700 \text{ m}$, $H_2 = 3300 \text{ m}$, and a reduced gravity $g' = 1.64 \times 10^{-2} \text{ m s}^{-2}$. As an aside, even though in the different trials the values of g' , H_1 , and H_2 change, we keep the value of a – obtained using g' , H_1 , and H_2 above – constant throughout. Other parameters used will be

as follows: $g = 9.81 \text{ m s}^{-2}$, and $\delta_2 \approx 0.0412$ as the canonical value for the open ocean used in Arbic et al. (2009). Thus, unless mentioned otherwise, we use the following values for all plots: $\alpha \approx 0.0017$, $\varepsilon \approx 0.345$, and $\gamma = 0.175$. In addition, we set $H_0 = 2,350 \text{ m}$ and $\sigma = 1$. The value of H_0 was chosen so that the ratio of the spatial and temporal averaged square of the upper layer and lower layer velocity in our finite basin control case (ratio ≈ 2.5) is approximately equal to the value obtained for these parameters in the global $1/8^\circ$ simulations discussed in section 2.

For each basin type we consider four trials: one layer solution, two layer solution (referred to as control) with $\alpha \approx 0.0017$, two layer solution with $\alpha \approx 0.0018$, and two layer solution with $\alpha \approx 0.0017$ – as in the control – but with $\gamma = 0.2$. In this way, the trials cover the cases of unstratified flow, stratified flow, perturbation of the layers’ densities, and perturbation in the layers’ thicknesses; as in Figures 1 and 2. We obtain $\alpha \approx 0.0018$ by assigning $g' = 1.78 \times 10^{-2} \text{ m s}^{-2}$ and $\gamma = 0.2$ by assigning $H_1 = 800 \text{ m}$. These values of α and γ are intended to represent climatic perturbations to the values of g' and H_1 . The interface perturbation is motivated by Figure 10 of Arbic and Owens (2001), which shows $\sim 100 \text{ m}$ displacements of isopycnals over decadal timescales in hydrographic observations of the North Atlantic. The g' perturbation was estimated from the $0.5^\circ\text{C century}^{-1}$ nominal maximum warming trend found in intermediate depth waters in the same paper. We computed the change in g' (with potential densities referenced to 1780 db) that would take place if a water parcel at 100 db having salinity 37 psu and temperature of 20°C warmed by 0.5°C . The deep reference parcel has depth of 3000 db, salinity 34.5 psu and temperature of 4°C .

The surface elevation amplitudes for the finite basin are presented in Figure 4, and the phases are presented in Figure 5. Similarly, the amplitudes for the infinite basin are presented in Figure 6, and the phases in Figure 7. For all figures the surface elevation is given by a solid red line and the barotropic component of the surface elevation is given by a solid blue line. We next explain

the setup of figures for the finite basin; the setup in the infinite basin is the same. Figures 4 (a) and 5 (a) show the one layer solution. Figures 4 (b) and 5 (b) show the difference between the two layer control, $\alpha \approx 0.0017$, and the one layer solution. Figures 4 (c) and 5 (c) show the difference between a two layer solution with a climatically perturbed $\alpha \approx 0.0018$ and the control two layer solution. Lastly, Figures 4 (d) and 5 (d) show the difference between a two layer solution with a climatically perturbed $\gamma = 0.2$ and the two layer control. The plots in Figure 8 are as in Figure 4 (b), (c), and (d) but with changes represented as percentages of the barotropic mode solution of the one-layer control case.

Lastly, we briefly bring up a point which will not be pursued further. For the purposes of this paper, all solutions were found using the Neumann series (Green's function) method except for the finite basin one-layer solution, RMS plots in Figure 9 and the resonance plot in Figure 10 where, instead, the Fourier series expansion was used. Figures 9 and 10 will be described in detail in the next section. For the topography used, the Fourier series solution was more numerically reliable. The numerical accuracy of all solutions was confirmed by checking that they satisfy the original set of differential equations.

b. Discussion

Consistent with the numerical results shown in Figures 1 and 2, plots of the full solution on a finite domain basin show that changes to the stratification lead to changes in the surface elevation's amplitude of order 2 – 10%, see Figures 4 and 8, while changes in the phase of the solution are of order 2 – 3 degrees, see Figure 5. The addition of a second layer to the finite basin model yields an observable change in the barotropic surface tidal elevation amplitude of up to 1.5% compared with the one layer case; see Figures 4 (b) and 8 (a). A climatic perturbation in α to the two layer solution may induce a further change in the barotropic mode's amplitude of about 3%; see Figures

4 (c) and 8 (b). Climatic perturbations in γ may induce qualitatively similar responses from the system; see Figures 4 (d) and 8 (c). Perturbations in α or γ may lead to an increase or a decrease in the barotropic mode's amplitude comparable in magnitude to the amplitude perturbation of the baroclinic mode. From inspection of solutions with different topographic amplitudes (not shown here for the sake of brevity), we find that stratification perturbations can yield either an increase or decrease in the barotropic mode, depending sensitively on the topography.

For an infinite basin, changes to the stratification parameters may cause changes to the solution's amplitude as high as 10%, see Figure 6, while changes in the phase of the solution are up to 4 degrees, see Figure 7. As opposed to the finite basin, quite noticeable in all amplitude plots is the apparent lack of a measurable effect on the barotropic mode. Closer inspection shows that the barotropic mode indeed changes, but these changes are an order of magnitude smaller than those in the baroclinic mode's amplitude and hence are not easily observable; see Figure 6 (b). Lastly, changes brought about by perturbing either of the stratification parameters, α or γ , may lead to qualitatively similar responses in the system's amplitude; compare Figures 6 (c) and (d).

A more global view of the sensitivity of the solution to the stratification parameter α can be obtained by computing the RMS value of relevant quantities as functions of α . Here we define the RMS value as

$$\varphi_{RMS} := \sqrt{\frac{1}{\ell_2 - \ell_1} \int_{\ell_1}^{\ell_2} |\varphi(x)|^2 dx}. \quad (68)$$

Figure 9 shows the RMS values – using the same parameter values as our two layer control – for four variables: U^{BT} , U^{BC} , N_1^{BT} , and N_1^{BC} . The plots show strong sensitivity in the form of oscillations of significant amplitude reinforcing the fact that the stratification affects the surface barotropic mode. In particular, for $\alpha \approx 0.0017$ – the α value of the two-layer control solution – we see that the barotropic RMS quantities may be perturbed as much as 10%; see black curves in Figures 9 (a) and (c). That is, the barotropic RMS values may change by as much as 10% from

peak to trough in the parameter range explored in this paper. It is worth noting that the observed oscillations are not about a constant mean; instead, the mean values in these plots vary with the stratification in an observable manner. This implies that these are not just oscillations about the limiting one-layer case. It is also observed that the sensitivity of the system to stratification is more significant when only the bottom layer is damped (black curves) than when both the top and bottom layers are identically damped (red curves). The greater sensitivity in the black versus red curves implies that the tidal sensitivity to stratification is itself sensitive to assumptions about how tidal energy is dissipated.

Some understanding of the sensitivity of this system to stratification can be obtained from a resonance plot in the same vein as those in Arbic et al. (2009). As in that paper, the quantity $\frac{1}{\varepsilon\pi}$ acts as a non-dimensional measure of the forcing frequency of the system with higher values equivalent to faster forcing. Figure 10 shows that, for our chosen parameters, the control solution lies near a resonance peak of the system. That is, the plot shows that effects of stratification on the barotropic surface tidal elevation might be accentuated due to our chosen location in parameter space.

6. Summary

We have presented an analytical tide model which demonstrates the impacts of stratification on surface tidal elevations in a qualitatively similar manner as in the global numerical simulations shown in Arbic et al. (2004), Shriver et al. (2014), and section 2. Our analytical and numerical results demonstrate the potential for the presence of stratification to impact the barotropic tide, and for climatic perturbations of oceanic stratifications to contribute to the secular changes in tides observed in tide gauge records. Our derived analytical formulas for the barotropic and baroclinic modal contributions to surface tidal elevations contain explicit dependence on the stratification

parameters α and γ , implying that the barotropic as well as the baroclinic mode is affected by stratification. This dependence can be understood, at a basic level, by the fact that changes in stratification affect the speed of barotropic gravity wave propagation in the basin which in turn change the tidal amplitude. We quantify these effects with surface elevation plots in both finite and infinite basins over a Gaussian bump and plots of the root mean square values of model velocities and elevations using representative oceanic parameters. We find that, for the given parameters, our finite basin model's barotropic mode is much more affected by stratification than that of our infinite domain model. A significant contribution to this effect arises from the size of the topography and particularly the nearness of the basin boundaries. For the finite basin, changes in stratification change the barotropic tide by as much as 10%, making these perturbations of a size comparable to the baroclinic signal of the tide.

Acknowledgments. BKA and ANW gratefully acknowledge support from National Science Foundation (NSF) grants OCE-0924481 and OCE-0960820. IC and MCH gratefully acknowledge support from the Department of Boating and Waterways of the State of California, grant 08-106-105. PDM and ANW were partially supported by the NSF under grant DMS-1206131. JFM was supported by a Research Experience for Undergraduates (REU) supplement to OCE-0924481. We acknowledge Detlef Stammer for organizing a workshop on secular changes in tides, which provided additional inspiration for this study. Useful discussions with Peter Brominski, Bill Dewar, Gary Egbert, Ron Flick, Chris Garrett, Malte Müller, and Richard Ray are gratefully acknowledged. Numerical computations were performed on the High-Performance Computing (HPC) centers at Florida State University. BKA thanks Jordan Yao, Dan Voss, and Paul van der Mark for technical support on the HPC. Arbic et al. (2009) Arbic and Owens (2001)

References

- Arbic, B. K., S. T. Garner, R. W. Hallberg, and H. L. Simmons, 2004: The accuracy of surface elevations in forward global barotropic and baroclinic tide models. *Deep-Sea Res. II*, **51**, 3069–3101, doi:10.1016/j.dsr2.2004.09.014.
- Arbic, B. K., R. H. Karsten, and C. Garrett, 2009: On tidal resonance in the global ocean and the back-effect of coastal tides upon open-ocean tides. *Atmosphere-Ocean*, **47**, 239–266, doi:10.3137/OC311.2009.
- Arbic, B. K., and W. B. Owens, 2001: Climatic warming of Atlantic intermediate waters. *J. Clim.*, **14**, 4091–4108, doi:10.1175/1520-0442(2001)014<4091:CWOAIW>2.0.CO;2.
- Arbic, B. K., A. J. Wallcraft, and E. J. Metzger, 2010: Concurrent simulation of the eddying general circulation and tides in a global ocean model. *Ocean Modelling*, **32**, 175–187, doi:10.1016/j.ocemod.2010.01.007.
- Cartwright, D. E., 1971: Tides and waves in the vicinity of Saint Helena. *Phil. Trans. R. Soc. Lond. A*, **270**, 603–646, doi:10.1098/rsta.1971.0091.
- Colosi, J. A., and W. Munk, 2006: Tales of the venerable Honolulu tide gauge. *J. Phys. Oceanogr.*, **36**, 967–996, doi:10.1175/JPO2876.1.
- Egbert, G. D., R. D. Ray, and B. G. Bills, 2004: Numerical modeling of the global semidiurnal tide in the present day and in the last glacial maximum. *J. Geophys. Res.*, **109** (C3), doi:10.1029/2003JC001973.
- Flick, R. E., J. F. Murray, and L. C. Ewing, 2003: Trends in united states datum statistics and tide range. *J. Waterway, Port, Coastal and Ocean Engin.*, **129**, 155–164, doi:10.1061/(ASCE)0733-950X(2003)129:4(155).

- Flierl, G. R., 1978: Models of vertical structure and the calibration of two-layer models. *Dyn. Atmos. Oceans*, **2**, 341–381, doi:10.1016/0377-0265(78)90002-7.
- Gill, A. E., 1982: *Atmosphere-Ocean Dynamics*. Academic Press, 662 pp.
- Greenberg, M. D., 1971: *Application of Green's Functions in Science and Engineering*. Prentice-Hall Inc., 141 pp.
- Hallberg, R., and P. Rhines, 1996: Boundary-driven circulation in an ocean basin with isopycnals intersecting the sloping boundary. *J. Phys. Oceanogr.*, **26**, 914–940, doi:10.1175/1520-0485(1996)026<0913:BDCIAO>2.0.CO;2.
- Hendershott, M. C., 1972: The effects of solid earth deformation on global ocean tides. *Geophys. J. Royal Astr. Soc.*, **29**, 389–402, doi:10.1111/j.1365-246X.1972.tb06167.x.
- Jay, D. A., 2009: Evolution of tidal amplitudes in the eastern pacific ocean. *Geophys. Res. Lett.*, **36**, L04 603, doi:10.1029/2008GL036185.
- Jayne, S. R., and L. C. St. Laurent, 2001: Parametrizing tidal dissipation over rough topography. *Geophys. Res. Lett.*, **28**, 811–814, doi:10.1029/2000GL012044.
- Kang, S. K., M. G. G. Foreman, H.-J. Lie, J.-H. Lee, J. Cherniawsky, and K.-D. Yum, 2002: Two-layer tide modeling of the Yellow and East China seas with application to seasonal variability of the M_2 tide. *J. Geophys. Res.*, **107**, 6–1–6–18, doi:10.1029/2001JC000838.
- Khatiwala, S., 2003: Generation of internal tides in an ocean of finite depth: analytical and numerical calculations. *Deep-Sea Res. I*, **51**, 3–21, doi:10.1016/S0967-0637(02)00132-2.
- Llewellyn Smith, S. G., and W. R. Young, 2001: Conversion of the barotropic tide. *J. Phys. Oceanogr.*, **32**, 1554–1566, doi:10.1175/1520-0485(2002)032<1554:COTBT>2.0.CO;2.

- Müller, M., 2012: The influence of changing stratification conditions on barotropic tidal transport and its implications for seasonal and secular changes of tides. *Cont. Shelf Res.*, **47**, 107–118, doi:10.1016/j.csr.2012.07.003.
- Müller, M., B. K. Arbic, and J. X. Mitrovica, 2011: Secular changes in ocean tides: Observations and model results. *J. Geophys. Res.*, **116**, C05 013, doi:10.1029/2010JC006387.
- Müller, P., 2006: *The Equations of Oceanic Motions*. Cambridge University Press, 291 pp.
- Munk, W., 1997: Once again: Once again - tidal friction. *Progress in Oceanography*, **40**, 7–35, doi:10.1016/S0079-6611(97)00021-9.
- Ray, R. D., 1999: A global ocean tide model from TOPEX/POSEIDON altimetry: GOT99.2, National Aeronautics and Space Administration technical memorandum. Tech. rep. NASA/TM-1999-209478.
- Ray, R. D., 2006: Secular changes of the M_2 tide in the gulf of maine. *Continental Shelf Res.*, **26**, 422–427, doi:10.1016/j.csr.2005.12.005.
- Ray, R. D., 2009: Secular changes in the solar semidiurnal tide of the western North Atlantic Ocean. *Geophys. Res. Lett.*, **36**, L19 601, doi:10.1029/2009GL040217.
- Ray, R. D., and G. T. Mitchum, 1996: Surface manifestation of internal tides generated near Hawaii. *Geophys. Res. Lett.*, **23**, 2101–2104, doi:10.1029/96GL02050.
- Ray, R. D., and G. T. Mitchum, 1997: Surface manifestation of internal tides in the deep ocean: observations from altimetry and island gauges. *Progress in Oceanography*, **40**, 135–162, doi:10.1016/S0079-6611(97)00025-6.

- Shriver, J. F., J. G. Richman, and B. K. Arbic, 2014: How stationary are the internal tides in a high-resolution global ocean circulation model? *J. Geophys. Res.*, **119**, 2769–2787, doi:10.1002/2013JC009423.
- St. Laurent, L. C., S. Stringer, C. Garrett, and D. Perrault-Joncas, 2003: The generation of internal tides at abrupt topography. *Deep-Sea Res. I*, **50**, 987–1003, doi:10.1016/S0967-0637(03)00096-7.
- Woodworth, P. L., 2010: A survey of recent changes in the main components of the ocean tide. *Continental Shelf Res.*, **30**, 1680–1691, doi:10.1016/j.csr.2010.07.002.
- Woodworth, P. L., S. M. Shaw, and D. L. Blackman, 1991: Secular trends in mean tidal range around the British Isles and along the adjacent European coastline. *Geophys. J. Int.*, **104**, 593–609, doi:10.1111/j.1365-246X.1991.tb05704.x.
- Zaron, E. D., and D. A. Jay, 2014: An analysis of secular change in tides at open-ocean sites in the pacific. *J. Phys. Oceanogr.*, doi:10.1175/JPO-D-13-0266.1, in press.

LIST OF FIGURES

Fig. 1.	Surface elevation amplitudes (cm) in $1/8^\circ M_2$ simulations: (a) one-layer control simulation, (b) two-layer control simulation minus one-layer control simulation, (c) two-layer “interface perturbation” simulation (with layer interface at 800 m) minus two-layer control simulation (with layer interface at 700 m), (d) two-layer “ g' perturbation” simulation with perturbed g' value of $1.78 \times 10^{-2} \text{ m s}^{-2}$ minus two-layer simulation with control g' value of $1.64 \times 10^{-2} \text{ m s}^{-2}$	33
Fig. 2.	As in Figure 1 but for phase of surface elevations (degrees) in $1/8^\circ M_2$ simulations.	34
Fig. 3.	Sketch of analytical two-layer model.	35
Fig. 4.	Surface elevation (red line) and barotropic surface elevation (blue line) amplitudes in a finite basin. Plot (a) was obtained using the Fourier series method while (b), (c), and (d) were obtained using the Neumann series method. The y-axis in all plots is non-dimensional amplitude. The range in the vertical scales of (b), (c), and (d) is identical.	36
Fig. 5.	As in Figure 4, but for phase differences in degrees. The large phase differences in the center of the basin are not very meaningful since these are associated with small amplitudes; see Figure 4 (a). The range in the vertical scales of (b), (c), and (d) is identical.	37
Fig. 6.	Surface elevation (red line) and barotropic surface elevation (blue line) amplitudes in an infinite basin. All plots were obtained using the Neumann series method. The y-axis in all plots is non-dimensional amplitude. The range in the vertical scales of (b), (c), and (d) is identical.	38
Fig. 7.	As in Figure 6, but for phase differences in degrees. The range in the vertical scales of (b), (c), and (d) is identical.	39
Fig. 8.	Surface elevation (red line) and barotropic surface elevation (blue line) amplitudes in a finite basin as a percentage of the control solution. All plots were obtained using the Neumann series method. As in Figure 5 the large differences in the center of the basin are not as meaningful. The range in the vertical scales of all plots is identical.	40
Fig. 9.	RMS values versus stratification parameter α for two layers damped ($\delta_1 = \delta_2 \neq 0$), in red, and only the bottom layer damped ($\delta_1 = 0, \delta_2 \neq 0$), in black. All plots were obtained using the Fourier series method.	41
Fig. 10.	Maximum value of the surface elevation amplitude N_1 versus non-dimensional forcing frequency for the Gaussian topography described in section 5. Red dot indicates position in parameter space for the control solution. Plot obtained using the Fourier series method.	42

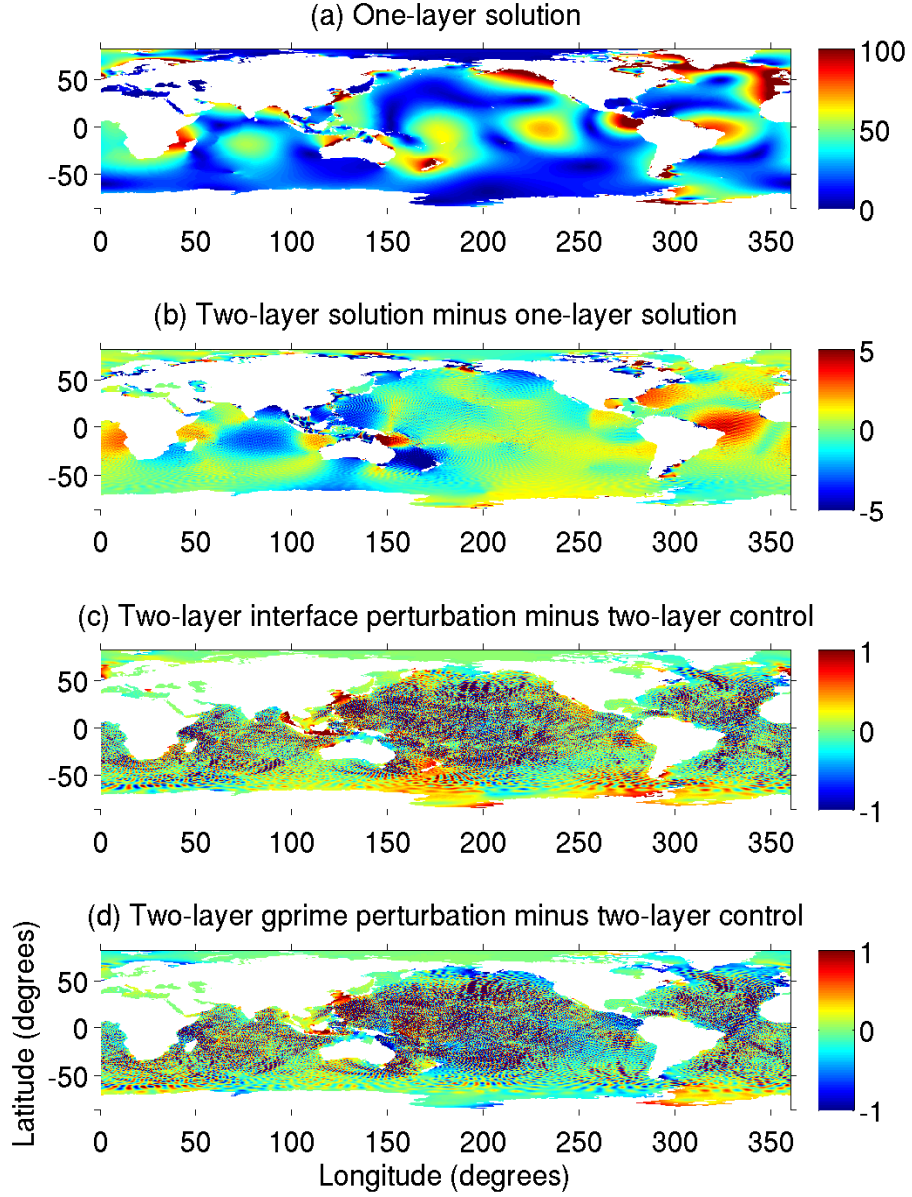


FIG. 1. Surface elevation amplitudes (cm) in $1/8^\circ$ M_2 simulations: (a) one-layer control simulation, (b) two-layer control simulation minus one-layer control simulation, (c) two-layer “interface perturbation” simulation (with layer interface at 800 m) minus two-layer control simulation (with layer interface at 700 m), (d) two-layer “ g' perturbation” simulation with perturbed g' value of $1.78 \times 10^{-2} \text{ m s}^{-2}$ minus two-layer simulation with control g' value of $1.64 \times 10^{-2} \text{ m s}^{-2}$.

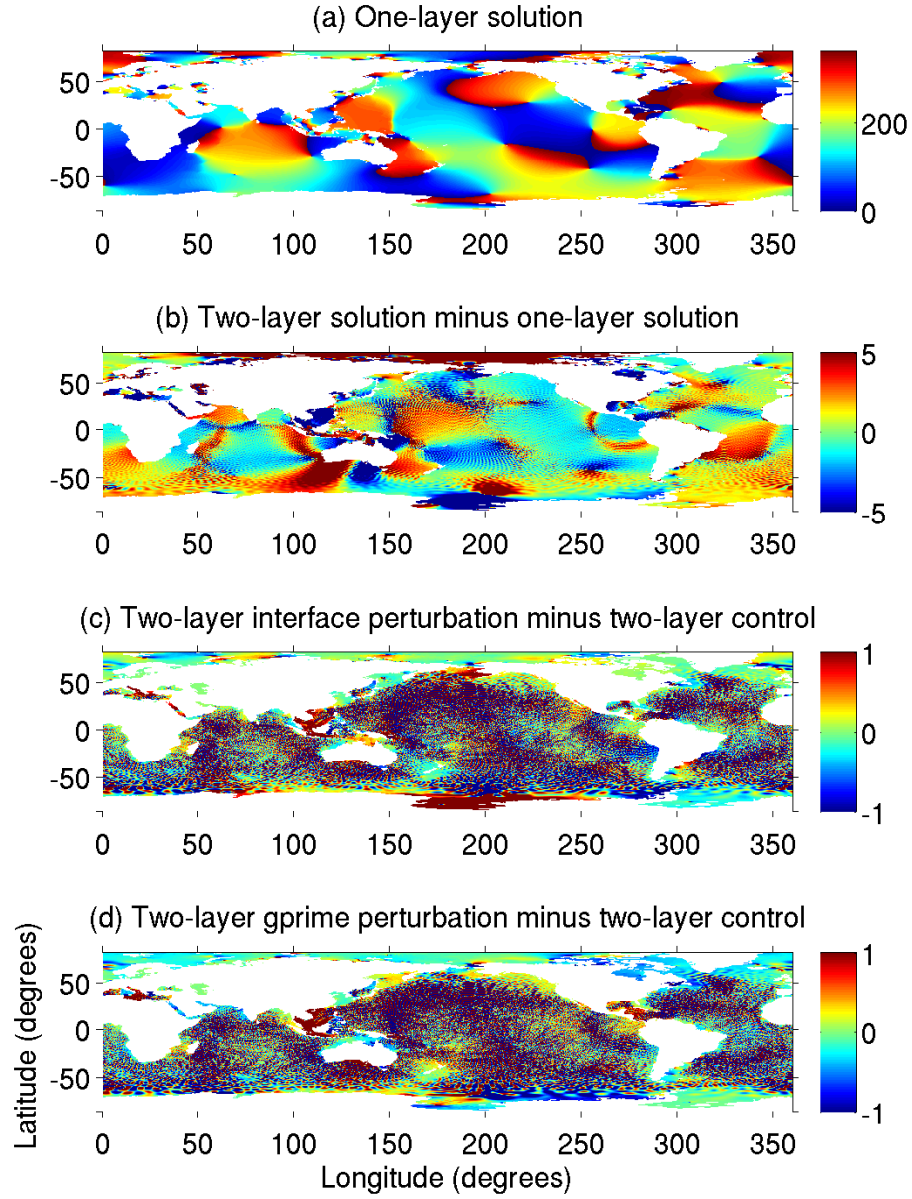


FIG. 2. As in Figure 1 but for phase of surface elevations (degrees) in $1/8^\circ M_2$ simulations.

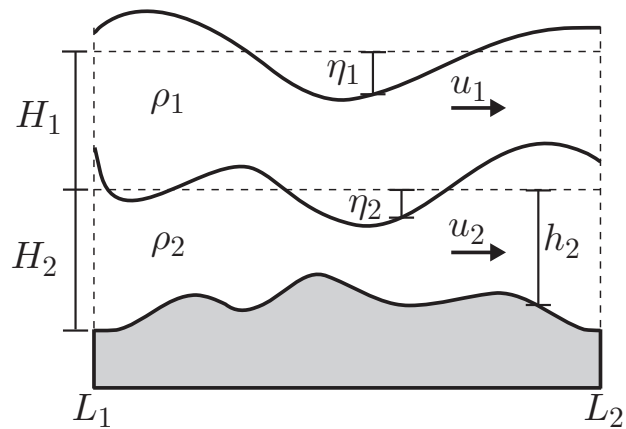


FIG. 3. Sketch of analytical two-layer model.

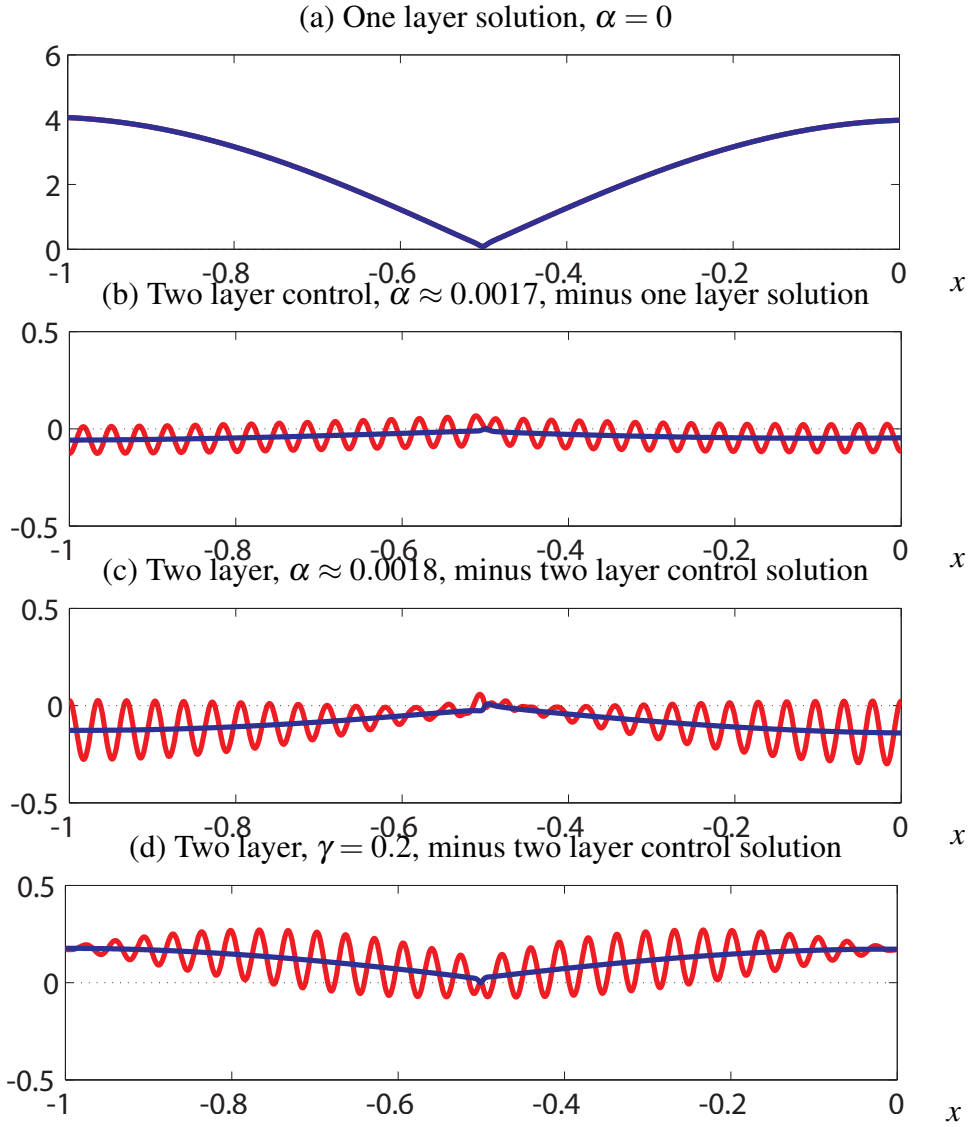


FIG. 4. Surface elevation (red line) and barotropic surface elevation (blue line) amplitudes in a finite basin. Plot (a) was obtained using the Fourier series method while (b), (c), and (d) were obtained using the Neumann series method. The y-axis in all plots is non-dimensional amplitude. The range in the vertical scales of (b), (c), and (d) is identical.

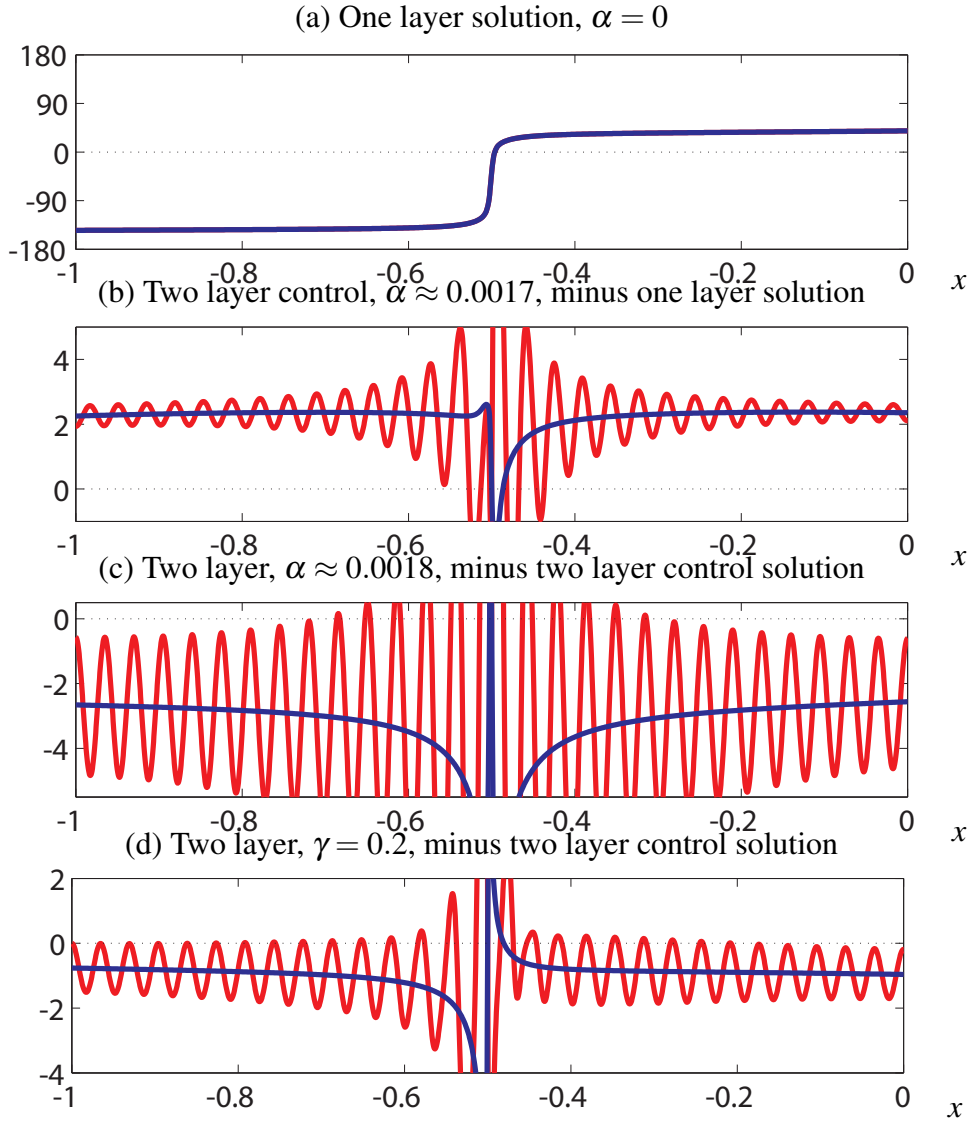


FIG. 5. As in Figure 4, but for phase differences in degrees. The large phase differences in the center of the basin are not very meaningful since these are associated with small amplitudes; see Figure 4 (a). The range in the vertical scales of (b), (c), and (d) is identical.

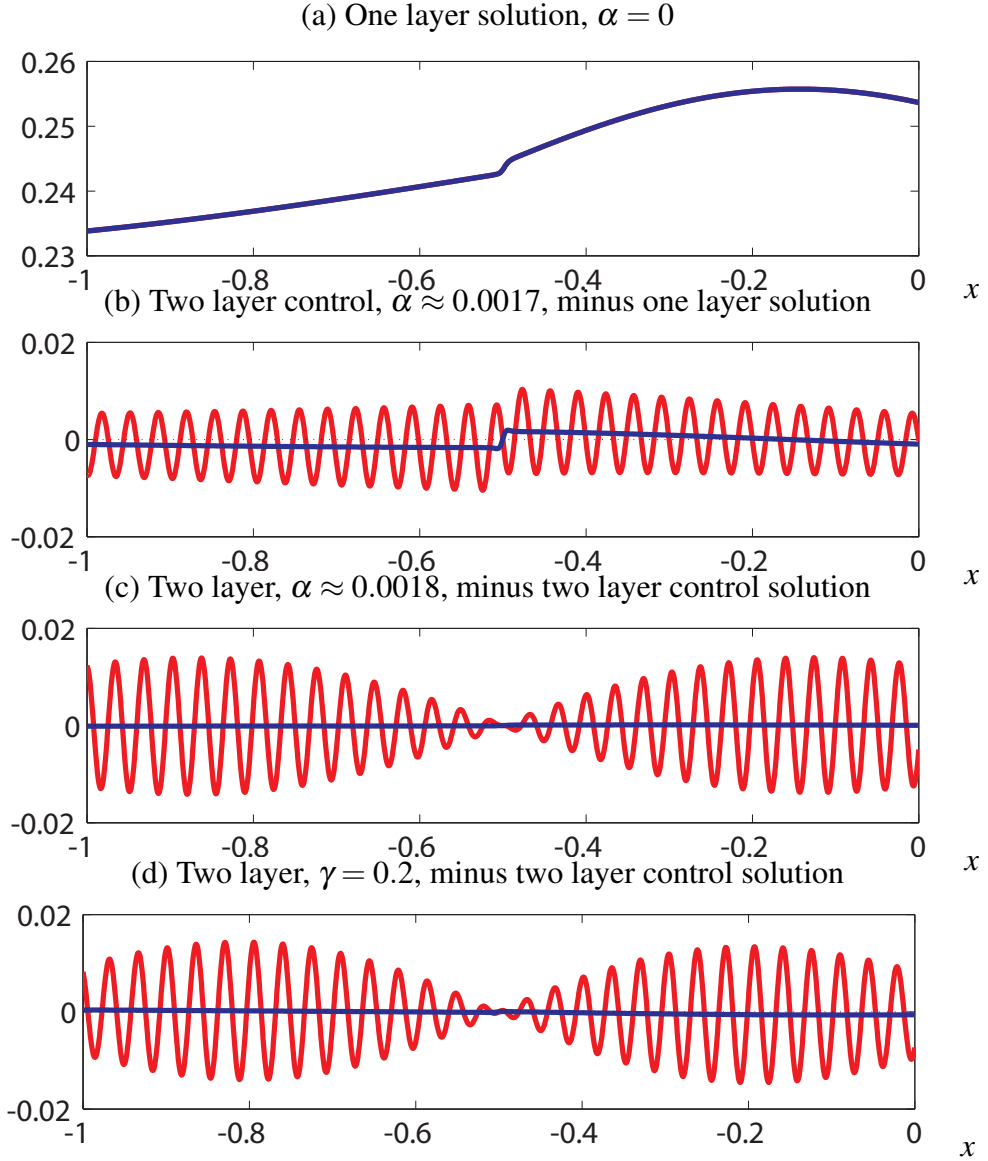


FIG. 6. Surface elevation (red line) and barotropic surface elevation (blue line) amplitudes in an infinite basin. All plots were obtained using the Neumann series method. The y-axis in all plots is non-dimensional amplitude. The range in the vertical scales of (b), (c), and (d) is identical.

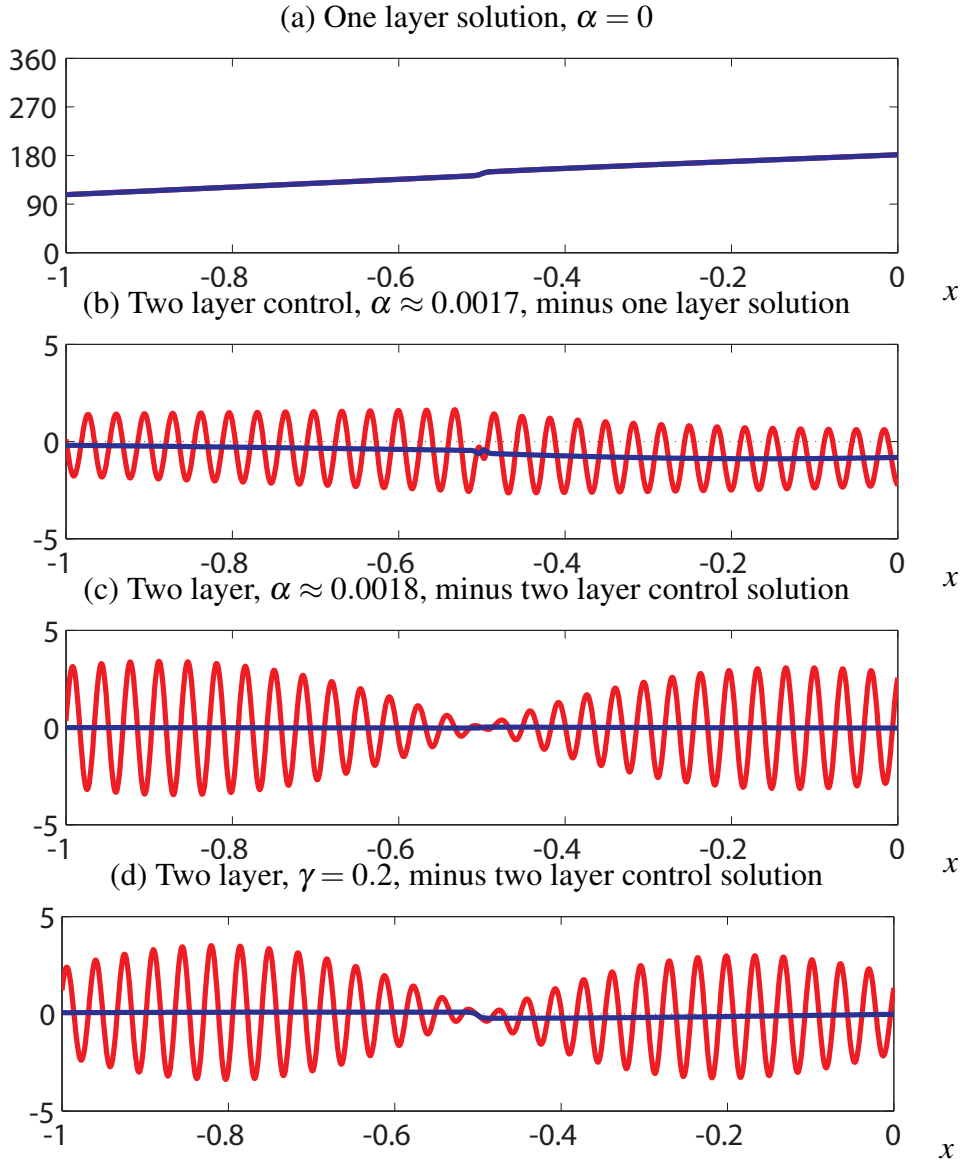


FIG. 7. As in Figure 6, but for phase differences in degrees. The range in the vertical scales of (b), (c), and (d) is identical.

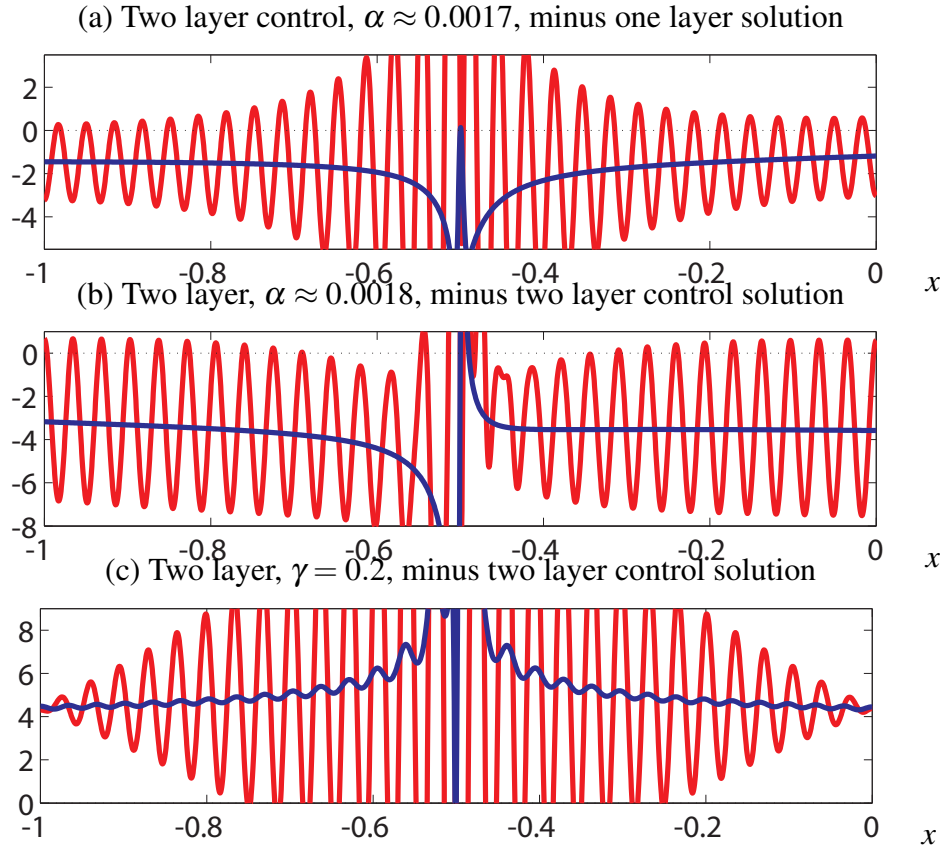


FIG. 8. Surface elevation (red line) and barotropic surface elevation (blue line) amplitudes in a finite basin as a percentage of the control solution. All plots were obtained using the Neumann series method. As in Figure 5 the large differences in the center of the basin are not as meaningful. The range in the vertical scales of all plots is identical.

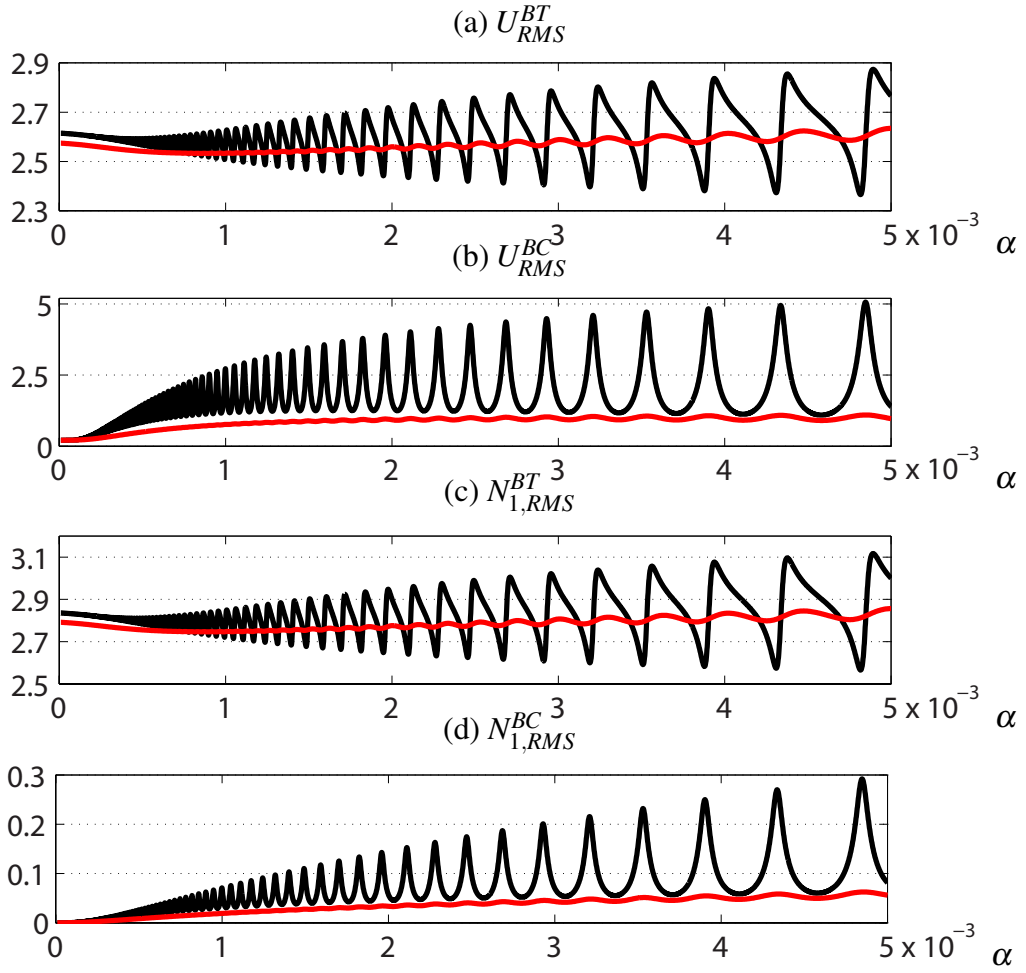


FIG. 9. RMS values versus stratification parameter α for two layers damped ($\delta_1 = \delta_2 \neq 0$), in red, and only the bottom layer damped ($\delta_1 = 0, \delta_2 \neq 0$), in black. All plots were obtained using the Fourier series method.

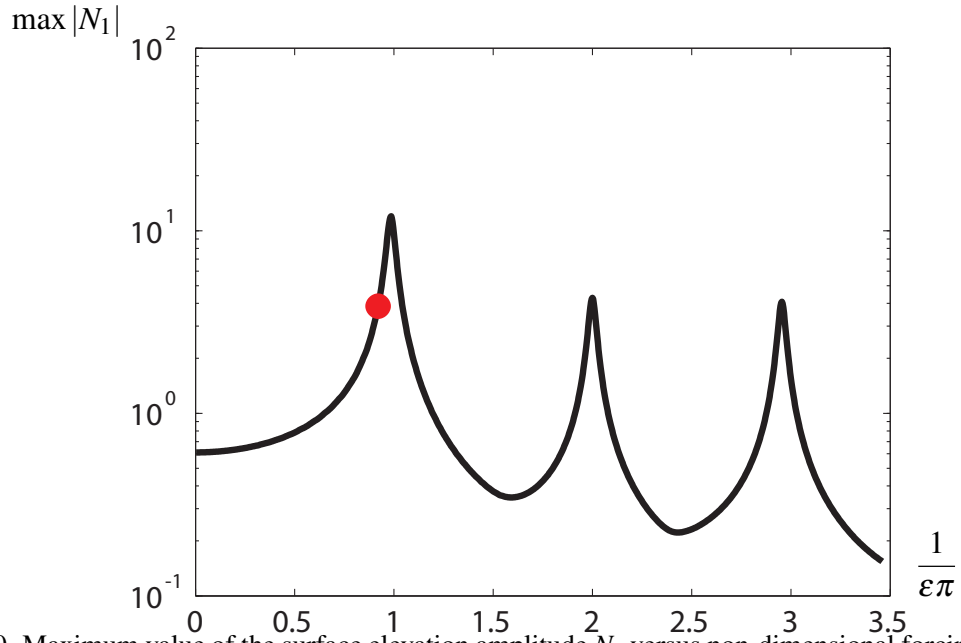


FIG. 10. Maximum value of the surface elevation amplitude N_1 versus non-dimensional forcing frequency for the Gaussian topography described in section 5. Red dot indicates position in parameter space for the control solution. Plot obtained using the Fourier series method.